

Selective Ionic Transport through Tunable Sub-Nanometer Pores in Single-Layer Graphene Membranes

*Sean C. O'Hern¹, Michael S. H. Boutilier¹, Juan-Carlos Idrobo², Yi Song³, Jing Kong³,
Tahar Laoui⁴, Muataz Atieh⁴, and Rohit Karnik^{1*}*

¹Department of Mechanical Engineering, Massachusetts Institute of Technology,
Cambridge, MA 02139, USA.

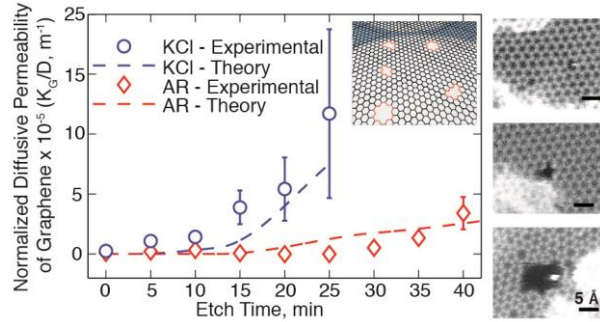
²Materials Science and Technology Division, Oak Ridge National Laboratory, Oak
Ridge, TN 37831, USA

³Department of Electrical Engineering and Computer Science, Massachusetts Institute of
Technology, Cambridge, MA 02139, USA

⁴Departments of Mechanical and Chemical Engineering, King Fahd University of
Petroleum and Minerals, Dhahran, Saudi Arabia

KEYWORDS. Molecular sieve, filter, ion selective membrane, desalination,
nanofiltration

Table of Contents Graphic:



ABSTRACT. We report selective ionic transport through controlled, high-density, sub-nanometer diameter pores in macroscopic single-layer graphene membranes. Isolated, reactive defects were first introduced into the graphene lattice through ion bombardment and subsequently enlarged by oxidative etching into permeable pores with diameters of 0.40 ± 0.24 nm and densities exceeding 10^{12} cm⁻², while retaining structural integrity of the graphene. Transport measurements across ion-irradiated graphene membranes subjected to *in situ* etching revealed that the created pores were cation-selective at short oxidation times, consistent with electrostatic repulsion from negatively charged functional groups terminating the pore edges. At longer oxidation times, the pores allowed transport of salt but prevented the transport of a larger organic molecule, indicative of steric size exclusion. The ability to tune the selectivity of graphene through controlled generation of sub-nanometer pores addresses a significant challenge in the development of advanced nanoporous graphene membranes for nanofiltration, desalination, gas separation, and other applications.

Graphene, an sp^2 -bonded allotrope of carbon, promises to be the backbone for a new class of highly permeable, highly selective molecular sieve material for both liquid-

phase¹⁻³ and gas-phase^{4, 5} separation processes. By creating sub-nanometer-sized pores in the otherwise impermeable two-dimensional lattice,⁶ graphene would act as a filter by permitting the transport of molecules smaller than the pores to pass through while significantly hindering the transport of molecules larger than the pores. Theoretical models predict that such a membrane would exhibit selectivity and permeability orders of magnitude greater than current state-of-the-art filtration membranes.^{1-4, 7, 8} However, experimental studies elucidating this behavior have thus far been limited. Due to the challenge of fabricating leak-free, large area, single-layer porous graphene membranes, transport measurements through graphene have been limited to microscopic areas with few pores⁹⁻¹² or multi-layered graphene-oxide (GO) membranes.¹³⁻¹⁶ In GO membranes, molecules travel a tortuous path through the interlayer region between flakes, and while such membranes have demonstrated selective transport, the measured permeability does not match the expected performance of porous single-layer graphene due to this longer path length.

Koenig *et al.*⁹ recently demonstrated selective gas transport through single- and double-layer graphene membranes of micron-scale areas with single or few pores. However, most experimental transport measurements through graphene pores have been performed for the purpose of DNA sensing where only ionic currents have been reported through isolated, single pores or uncontrolled defects.^{10-12, 17, 18} Pores used for DNA sensing are significantly larger than the sizes of many ions and molecules that are of interest in separation by reverse osmosis and nanofiltration. In all these studies, the membrane nanostructures that resulted in the observed transport properties were not characterized at the atomic level, and the relationship between graphene pore sizes and transport behavior

has so far remained elusive. Furthermore, in contrast to isolated pores, for practical applications selectivity must be imparted by multiple pores at sufficient densities acting in parallel over macroscopic areas of graphene.

The immense potential of porous, single-layer graphene membranes is therefore predicated on the ability to introduce controlled, sub-nanometer-sized pores at high density over large areas of graphene and to understand the relationship between pore structures and the resulting transport properties. Though irradiating graphene with a focused electron beam above the carbon knock-out potential (~ 80 kV) creates single, controlled pores of less than 2 nm,^{11, 12, 17} oxidative processes to create pores in graphene can be readily applied to large areas.^{9, 19-22} Exposure to high temperature atmospheric oxygen,²¹ ozone under ultraviolet light,^{9, 19} and hydrogen plasma²⁰ have been used to create pores in macroscopic areas of graphene. However, because grain boundaries are more reactive than the basal plane, oxidation processes typically lead to pores of widely varying sizes.²⁰ To obtain pores of controlled size and density, Russo *et al.*²³ addressed the difference between the reactivity of the basal plane and the grain boundaries by creating artificial defects in the basal plane through argon ion irradiation. Instead of using an oxidative process to enlarge the defects into pores, irradiation of the defective graphene with a diffuse electron beam at the carbon knock-out potential (~ 80 kV) was found to result in tightly distributed pore sizes. However, the pore generation process was still very limited in terms of membrane area and utility due to the use of a high-voltage electron beam for pore enlargement, and the stability of these pores as well as their transport characteristics remain unknown.

In this paper, we report a simple technique to create controlled, high-density, sub-nanometer diameter pores over macroscopic areas of single-layer graphene synthesized by chemical vapor deposition (CVD) and investigate the ionic transport behavior of these pores. We first nucleate reactive, isolated defects in graphene through ion bombardment and then grow them into permeable pores using oxidative etching (Fig. 1). Through diffusion measurements of potassium chloride and an organic dye, we demonstrate control over the selectivity of single-layer graphene membranes at the sub-nanometer length scale.

Graphene synthesized on copper *via* low-pressure CVD was transferred to a holey-carbon transmission electron microscope (TEM) grid using the procedure described in ref.²⁴ (see Methods for details). The ratio of the intensity of the G' peak ($\sim 2700\text{ cm}^{-1}$) to the G peak ($\sim 1580\text{ cm}^{-1}$) ($I_{G'}/I_G \sim 3$) and the ratio of the intensity of the D peak ($\sim 1350\text{ cm}^{-1}$) to the G peak ($I_D/I_G \sim 0$) in the Raman spectrum indicated primarily single layer graphene with few defects (Fig 2a). Images of the graphene using aberration-corrected scanning transmission electron microscopy (STEM) confirmed these results (Fig. 3a). To seed pore growth, we artificially introduced reactive defects^{20, 25} into the graphene by bombarding the graphene with gallium ions at a density of $\sim 6 \times 10^{12}$ ions cm^{-2} with 8 kV acceleration voltage and 52° incident angle that is predicted to have a high probability ($\sim 80\text{-}90\%$) of each impact site producing a basal-plane defect.²⁶ To enlarge the artificial defects into selectively permeable pores, the graphene was etched in acidic potassium permanganate (1.875 mM KMnO_4 in 6.25% H_2SO_4), an oxidant known to attack unsaturated carbon bonds^{27, 28} and unzip carbon nanotubes²⁹.

Consistent with earlier simulations²⁶ and experiments,²³ the bombardment process introduced defects into the lattice as indicated by the appearance of distinct defect-related peaks in the Raman spectrum³⁰ (D peak at $\sim 1350\text{ cm}^{-1}$ and D' peak at $\sim 1620\text{ cm}^{-1}$) (Fig. 2b) and the emergence of many sub-nanometer sized pores in ion-bombarded and etched graphene observed using the STEM (Fig. 3d-f). In the absence of ion bombardment no pores were observed in the graphene (Fig. 3a-c) and the Raman spectra remained relatively unaltered compared to pristine graphene (Fig. 2a), demonstrating that nucleation of defects through ion bombardment was critical for creation of the pores. Interestingly, very few defects were visible in the STEM images of the ion-bombarded graphene before etching (Fig. 3d), which may be due to defect migration³¹ during the annealing step necessary for STEM imaging (see Methods) and the propensity of defects to attract hydrocarbon contamination during imaging.³² The appearance of pores in the STEM images after etching may reflect stabilization of the pores through chemical functionalization that mitigates their migration during the anneal step.

Analysis of $\sim 74,000\text{ nm}^2$ area of graphene imaged for etch times ranging from 0 – 120 min revealed a lognormal distribution of pore sizes (Fig. 4a) with an increase in their density as the etching progressed (Fig. 4b) (see Methods). After 120 min of etching, the pore density approached the theoretically predicted defect density expected from the ion bombardment process²⁶ ($\sim 80\%$ of the ion bombardment density of $\sim 6 \times 10^{12}\text{ ions cm}^{-2}$). The direct correlation between the observed pore density and the ion bombardment density at long etch times, and the lack of pores in the non-bombarded graphene suggest that the presence of defects is essential for growth of pores and that the observed pores originate by enlargement of defects induced by ion bombardment. Since ion

bombardment density greatly exceeds the density of intrinsic defects, we expect that the pore density will never significantly exceed the ion bombardment density, though additional pores may develop from intrinsic defects and grain boundaries, albeit at a much lower density than the ion bombardment density. This increase in pore density was coincident with degradation of the sp^2 -bonds as indicated by a concomitant decrease in the G' peak at 2700 cm^{-1} in the Raman spectrum³⁰ (Fig. 2b). Although the pore density increased with etch time, the mean pore diameter increased significantly only during the first 30 min and then appeared to stabilize at $0.40\pm 0.24\text{ nm}$ at the 60 min etch time (Fig. 4c).

These two observations – increase in pore density without significant increase in pore size, and stabilization of the pore size – indicate a slow, stochastic initiation of the reaction at the nucleated defect followed by rapid growth till the pore size is stabilized around 0.4 nm. Empirical simulations of pores modeling this growth behavior resulted in pore size distributions that evolved in a manner similar to the experimentally observed pore size distribution, confirming this hypothesis (see Supplementary Information Section II). This behavior suggests that there is a high initial barrier to the reaction, but this barrier is lowered once the reaction commences, causing rapid growth of the pore. As the pore grows, stabilization of the edge of the pore by functional groups^{29, 33} may again slow down the reaction. XPS analysis revealed the appearance of C=O and C-O bonding after exposure to the etch solution (Fig. 4d), suggesting that the pore edges were terminated by ketone, quinone, hydroxyl, or carboxyl groups.^{29, 33-35} The lognormal distribution of pore sizes would then result from discrete etching events, possibly also influenced by heterogeneity in the initial defects and aggregation of smaller pores into

larger pores at high pore densities. The mechanism of the etching reaction and the reason for the stabilization of the pore size is not fully understood and requires further investigation. Regardless, stabilization of pore size allows for a tighter distribution of pore diameters than that possible in case of a linear growth rate, and also results in sub-nanometer pores that are predicted to exhibit the selectivity required for nanofiltration, desalination, and gas separation.¹⁻⁵

To investigate transport across the created pores, we fabricated a graphene composite membrane (GCM) by direct transfer of graphene from copper foil³⁶ to a polycarbonate track etch (PCTE) membrane support²⁴ (Fig. 5a and Fig. 5b) (see Methods). After transfer, the graphene was bombarded with gallium ions using the same procedure as described above, and a series of diffusion measurements were performed alternating with *in situ* exposure to the permanganate etch solution (see Methods). Before etching, we observed some transport of potassium chloride (KCl, $d_{\text{KCl}} \sim 0.66$ nm) and a larger organic dye molecule (Allura Red AC, $d_{\text{AR}} \sim 1.0$) which was comparable to the transport in the non-bombarded GCM (Supplementary Fig. S5) and consistent with the presence of tears and defects in CVD graphene.²⁴ Additionally, the membrane potential was zero, indicating no selectivity between potassium and chloride ions (Fig. 5c).

Upon etching, both the membrane potential and the rate of KCl diffusion increased at the 5 min etch mark while the Allura Red transport remained constant (see Fig. 5c). The increase in membrane potential indicates the emergence of modest selectivity in the transport of the positively-charged potassium ion over the negatively-charged chloride ion. The observed selectivity is likely due to electrostatic interactions with the negative charges from the functional groups terminating the edge of the pore as predicted by

recent simulations.^{2, 3, 8} These measurements demonstrate that the nucleated defects were initially impermeable to both ions, but gradually became permeable to the potassium and chloride ions after exposure to the etchant. As the etching progressed the membrane potential slowly decayed to zero, indicating loss of selectivity between the potassium and chloride ions. Simultaneously, the transport of KCl across the GCM gradually increased and plateaued beyond the 25 min etch mark, while that of Allura Red remained essentially unchanged (Fig. 5c). These results demonstrate that as the created pores increased in size, the influence of electrostatic effects governing potassium/chloride ion selectivity diminished, yet steric effects dominated the transport behavior by excluding the larger Allura Red from diffusing across the graphene.

With further etching, transport of Allura Red started increasing and eventually saturated at etch times exceeding ~50 min. At the 120 min etch time, transport of KCl and Allura Red across the GCM was identical with that of just the support PCTE membrane without graphene (Supplementary Fig. S6), indicating that transport was limited by diffusion through the support PCTE membrane. In control experiments with a non-bombarded GCM, KCl transport increased only beyond the 30 min etch time, while Allura Red transport started increasing only around 90 min of etch time (Supplementary Fig. S5). In the absence of nucleated defects, this increase in transport must occur through growth of pores that were likely developing at intrinsic point defects, grain boundaries, wrinkles, and amorphous regions³⁷ at densities too low to be detected by STEM or Raman spectroscopy. As the PCTE membrane has well-defined cylindrical pores, it is possible to extract the permeability K_G^{exp} [m s⁻²] of the created pores in the graphene defined by

$$j_G = K_G^{exp} \Delta C \quad (1)$$

where j_G [mol m⁻² s⁻¹] is the flux through the created graphene pores and ΔC [mol m⁻³] is the concentration gradient across the membrane. The permeability K_G^{exp} , is then estimated using a circuit analogy as

$$K_G^{exp} = \left[\left(\frac{\gamma}{1/R_{GCM} - (1-\gamma)/R_{PC}} \right) - R_{PC} \right]^{-1} - \frac{1}{R_I} \quad (2)$$

where $1 - \gamma$ is the fraction of PCTE membrane pores not covered by graphene²⁴, R_{GCM} is the measured transport resistance of the GCM, R_{PC} is the resistance of the PCTE membrane pore, and R_I is the measured resistance of the intrinsic holes in the graphene membrane²⁴ (see Supplementary Information Section IV-A for derivation). Equation 2 essentially calculates the contribution of the created pores above that of the defects already existing in the GCM. At the 25 min etch time, the permeability of the graphene to KCl due to the created pores normalized by the diffusivity (\pm S.D.) increased to $1.2 \pm 0.7 \times 10^6$ m⁻¹, while that of Allura Red remained essentially indistinguishable from zero (Fig. 5e), indicating selective transport of KCl through the created pores. Non-bombarded graphene still exhibited some selectivity due to intrinsic defects in the graphene being etched (Supplementary Fig. S5), peaking at the 60 min etch mark.

To verify that the created pores were responsible for the selective transport, we compared the experimentally determined permeability due to the created pores with the theoretical permeability estimated from the pore distributions observed in the STEM images, assuming continuum diffusion through independent pores in a membrane as

$$K_G^{th} = 2D \sum_{a_i > H} (a_i - H) / A_{PC} \quad (3)$$

where K_G^{th} is the theoretical permeability, D is the diffusivity of the molecule, A_{PC} is the area of the PCTE pore, a_i is the radius of the graphene pore, and H is the radius of the molecule (see Supplementary Information Section IV-C for derivation). Here, the theoretical etch times are divided in half as the graphene samples on the TEM grids were etched from one side and the graphene in the diffusion cell was etched from both (see Supplementary Information Section IV-D for further discussion). As presented in Figure 5e, the theoretical permeability of the pores created in the graphene matches well with the experimentally measured permeability. These results further suggest that the created pores are responsible for the GCM selectivity.

Interestingly, it appears the most important characteristic of the pore size distribution on the transport rate in the diffusion experiments reported here is not the mean pore size that is consistently less than the size of both the KCl and Allura Red, but the extent of the lognormal tail. The diffusive resistance of the graphene scales as $\sim D^{-1}$ while the diffusive resistance of the PCTE pore scales as $\sim LD^{-2}$, where D is pore diameter and L is pore length. Therefore, for Allura Red diffusion the graphene need only have $2 \times 10^{10} \text{ cm}^{-2}$ 1.8 nm diameter pores before the resistance of the graphene equals the resistance of the PCTE. The presence of a few large pores is therefore sufficient to diminish selectivity in the case of diffusive transport, which is always limited by the finite thickness of the support membrane. This results in the plateau in the transport rates observed in Figure 5c and the inability to extract transport properties of graphene once its permeability approaches that of the support (Fig. 5e). In contrast, the entire pore size distribution is expected to be relevant for pressure-driven flow where the transport resistance of the support will rarely exceed that of graphene due to a much stronger dependence on

diameter (D^{-3}). We can therefore anticipate that rather than just the tail, the entire pore size distribution will be relevant for these separations. However, pressure-driven measurements must await the development of techniques to mitigate leakage through defects.

In conclusion, we have developed a method to create controlled sub-nanometer-sized pores in large area single-layer graphene membranes through chemical oxidation of nucleated defects. Transport through these pores is highly selective and tunable by simply controlling the etch time. While stabilization of pore growth limits the range of pore sizes that can be created to within approximately 1 nm, the sub-nanometer to nanometer pore sizes obtained are in the right range for nanofiltration with applications including removal of organic contaminants, water softening, etc.³⁸ and potentially even for desalination¹. We anticipate that the flexibility to modify the pores through well-known conjugation chemistries^{39, 40} will further open new avenues for incorporating versatile functionality in these membranes. While we have used ion bombardment as a highly controllable method to induce defects,^{26, 41} growth of defects formed during graphene synthesis through doping⁴² or other methods^{9, 23} will further enhance the scalability of this approach. These results represent a significant advancement in the development and the future realization of nanoporous graphene-based membranes.

Methods

Materials. Graphene was grown on copper foil (JX Nippon Mining & Metals HA Foil) in a home-built system using Low-Pressure Chemical Vapor Deposition (LPCVD). First, the copper foil was placed in a quartz tube and annealed at 1000° C for 30 min in a hydrogen environment. Next, the graphene was grown for 30 min by increasing H₂ flow

rate to 70 sccm and setting the CH₄ flow rate to 0.5 sccm. The chamber pressure during the growth phase was 1.90 Torr. The growth conditions outlined above produces high-quality graphene with very few bilayer regions. Copper etchant used for transfers was APS-100 (10-20% ammonium persulfate, Transene). Target substrates for graphene transfers were Sterlitech non-PVP coated, hydrophobic, polycarbonate track etch (PCTE) membranes with 200 nm pores and gold 200 mesh Quantifoil Holey Carbon transmission electron microscope grids (TEM, Ted Pella, Inc.) with 1.2 μm diameter holes. Dyes and salts used in transport experiments were potassium chloride (KCl, Mallinckrodt Chemicals) and 98% Allura Red AC (Sigma-Aldrich).

Graphene transfer procedure. For STEM imaging and Raman microscopy, graphene was transferred to gold TEM grids (Ted Pella, Inc.) using the procedure described in ref.²⁴ For transport measurements, as-synthesized low pressure CVD graphene on copper was transferred to PCTE membranes (Sterlitech) with 200 nm pores using the procedure described in ref.²⁴. To perform XPS on graphene, graphene was first transferred to a Si/SiO₂ wafer using a sacrificial polymer transfer procedure similar to that described in ref.⁴³. Detailed procedure is described in Supplementary Information.

Ion bombardment. Ion bombardment was performed using a Helios Nanolab Dualbeam 600 at 8 kV and a current of 1.55-1.65 nA with a 52° angle of incidence. To achieve appropriate bombardment dose, a series of screenshots were captured over the entire graphene area (100× zoom, 4096×3536 pixels, dwell time of 1 μs pixel⁻¹, ~2.24 mm² area) spaced so as to minimize overlapping bombardment regions.

Scanning electron microscopy (SEM). SEM images were acquired on a Helios Nanolab Dualbeam 600 as described in ref.²⁴.

Scanning transmission electron microscopy (STEM). STEM imaging was performed on a Nion UltraSTEM 100tm⁴⁴ operated at 60 kV to ensure that no damage would be done to the graphene while imaging. Images were acquired using a convergence semiangle of 30 mrad and an annular dark field detector with ~54 to 200 mrad half-angle range. Before imaging, the samples were baked for 10 h under 10⁻⁵ torr at 160° C to decrease surface contamination. After cooling to room temperature under vacuum for about 10 h, they were immediately transferred to the STEM column. The images were filtered using a low-pass smoothing function implemented in the program ImageJ and the s-curve of the image was adjusted in Adobe Photoshop to increase the contrast between the graphene lattice and the holes. To compare the effect of etching on bombarded and non-bombarded graphene, a selected area (~3.5 mm²) of five different graphene samples was first bombarded with gallium ions using the prescribed procedure. Next, each sample was etched for 0, 5, 25, 60, or 120 min. Images were acquired at randomly selected points on both the bombarded and the non-bombarded areas of graphene for pore counting and diameter estimation. This allowed for direct comparison between the non-bombarded and bombarded graphene for a specified etch time.

Pore Diameter Estimation. Pore diameters were estimated manually by measuring the area, A_{pore} , of each pore using the polygon selection tool in ImageJ (see Supplementary Fig. S2 for example pores). Effective pore diameter was calculated as

$$d_{pore} = \sqrt{4A_{pore}/\pi} \quad (4)$$

The number of pores counted and the total imaged area for each etch time is tabulated in Supplementary Tables S1 and S2.

X-ray photoelectron spectroscopy (XPS). XPS measurements were carried out on a Thermo Scientific K-Alpha XPS at the Center for Nanoscale Systems. XPS spectrum was collected on samples at 45° incident angle with a 400 μm spot size integrated over 10 scans. Before analysis, the samples were annealed in a tube furnace for 4 h at 160 °C in a stream of argon to remove any residual organic contamination.

Raman spectroscopy. Raman spectra were acquired with a WiTec Alpha 300 Confocal Raman with a 532 nm source. Before capturing Raman spectra of graphene on TEM grids, samples were annealed in Ar at 160° C for 4 h to remove residual contamination. Care was taken to ensure that each Raman signal acquired was from suspended graphene on TEM grids. Each point was integrated over 120 s at low laser power to minimize laser damage and had a grating of 600 lines mm⁻¹ with a center wavevector of 2000 cm⁻¹.

Transport measurements. Transport measurements were carried out using a 3.4 mL Side-bi-Side glass diffusion cell with a 3 mm orifice (PermeGear, Inc.). KCl transport was measured by filling one side of the cell with 0.5 M KCl and monitoring the conductivity on the other side. Allura Red AC transport was measured using *in situ* UV-vis spectroscopy by filling one side of the cell with 1 mM solution in 0.5 M KCl and the other side with 0.5 M KCl to eliminate electrokinetic artifacts.²⁴ The membrane potential was extracted from the cell potential measured using Ag/AgCl electrodes with 0.5 M KCl and 0.1667 M KCl on either side of the membrane. Details of the transport measurements are given in Supplementary Information.

Figures

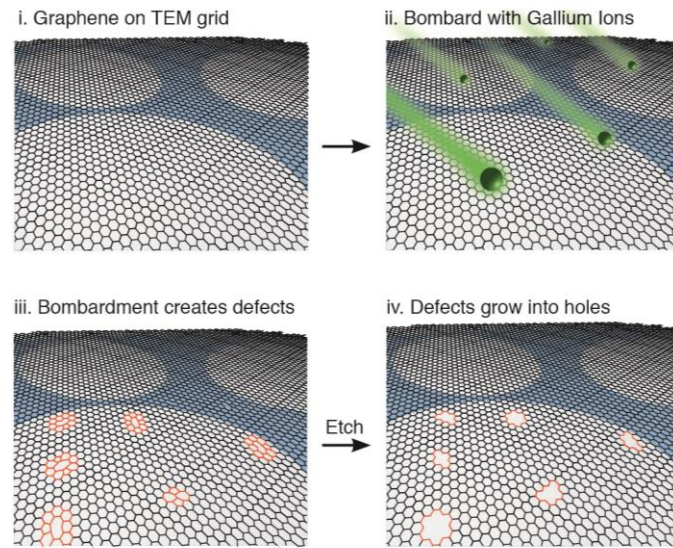


Figure 1. Process to create controlled pores in graphene membrane. Controlled sub-nanometer pores in graphene are created by ion bombardment followed by chemical oxidation. Ion bombardment generates reactive defect sites in the graphene lattice that preferentially etch during exposure to acidic potassium permanganate etchant.

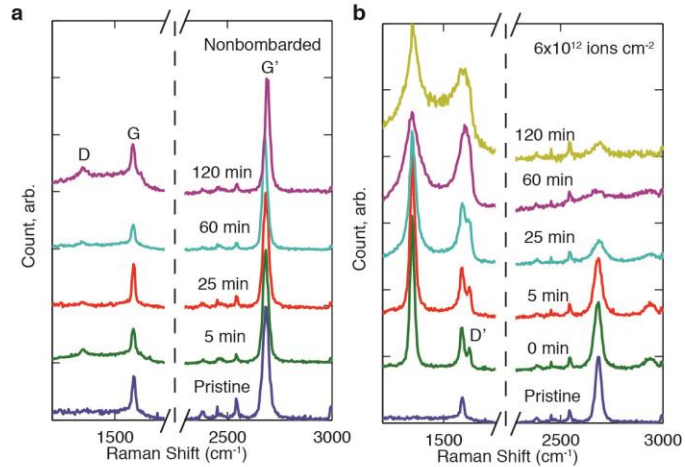


Figure 2. Raman spectrum of graphene membranes. a. Raman spectra of nonbombarded graphene indicates that etchant minimally effects pristine lattice. **b.** Raman spectra of pristine graphene and graphene bombarded and etched for 0 min, 5 min, 25 min, 60 min, and 120 min. Upon bombardment, an increase in the defect related Raman bands (D peak at $\sim 1350\text{ cm}^{-1}$ and D' peak at $\sim 1620\text{ cm}^{-1}$) demonstrate that although very few holes were found in STEM images of the graphene at 0 min, disorder was created. Upon etching, $I_{D'}/I_G$ decreases as the lattice slowly degrades.

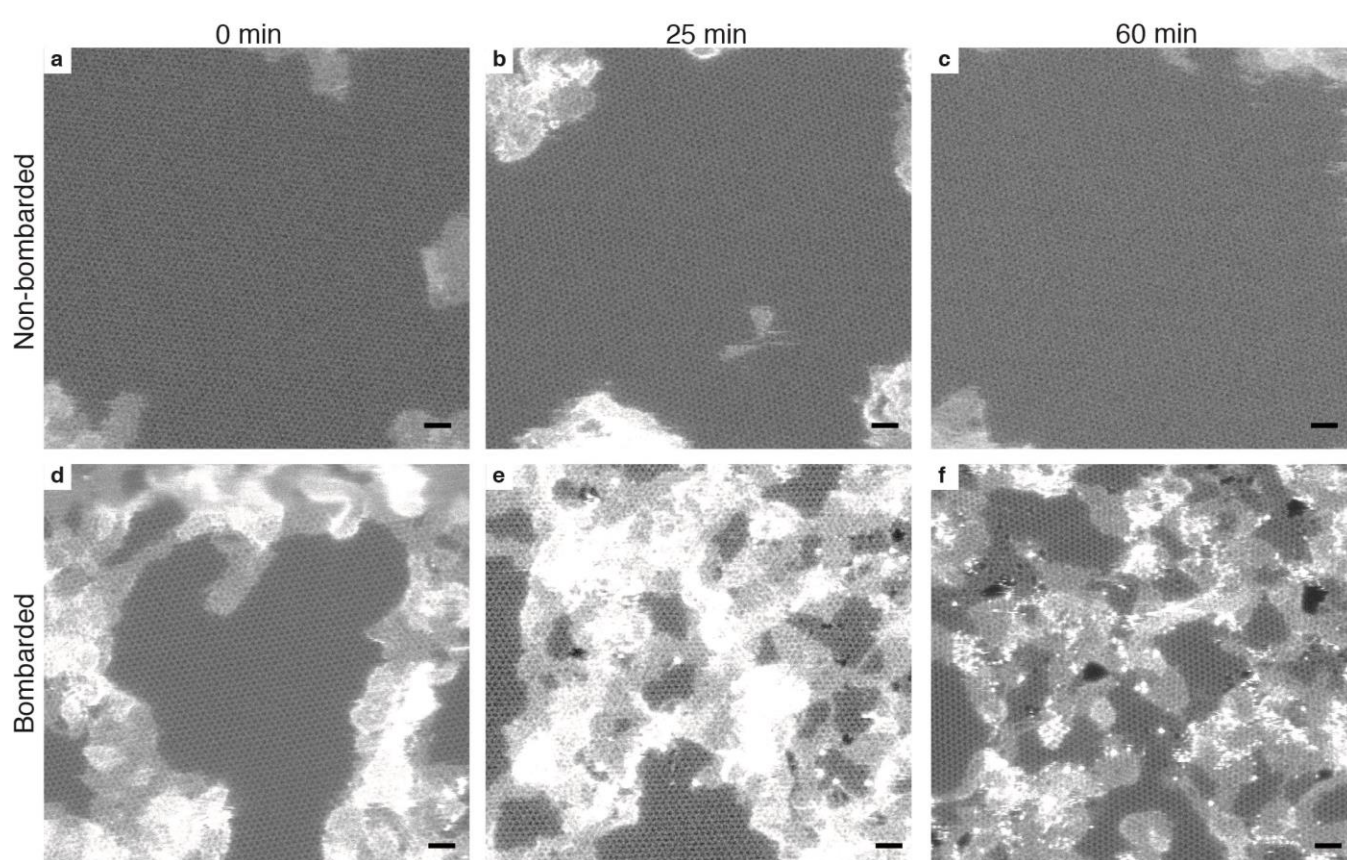


Figure 3. Scanning transmission electron micrographs of pores created in graphene membranes. Comparison between graphene etched in acidic potassium permanganate with (d, e, f) and without (a, b, c) ion bombardment demonstrates that both bombardment and etching are necessary for pore creation. Etch times are 0 min, 25 min, and 60 min. Scale bars are 1 nm. Additional images for 5 min and 120 min etch times presented in Supplementary Fig. S1.

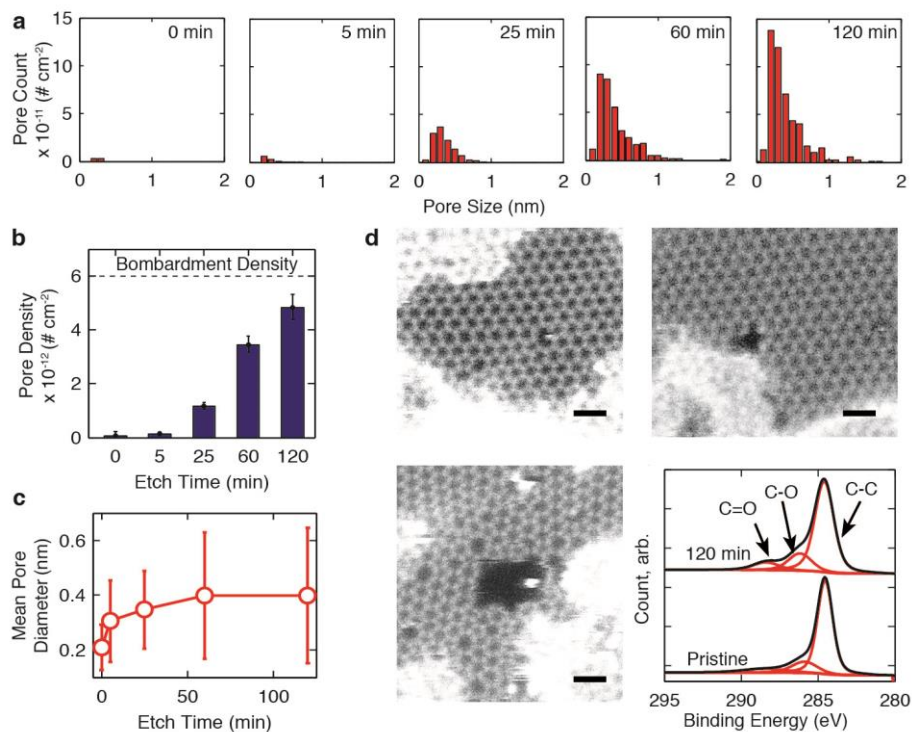


Figure 4. Analysis of pores in graphene membrane created through ion bombardment followed by acidic potassium permanganate oxidation. **a.** Distribution of pore sizes at 0 min, 5 min, 25 min, 60 min, and 120 min etch times. See Supplementary Section I-D for discussion of pore diameter estimation and Supplementary Fig. S2 for example measurements. **b.** Pore density of graphene nearly reaches bombardment density after etching for 120 min, suggesting that each ion impact seeds a defect site, yet initiation of pore growth is stochastic. **c.** Growth of mean pore diameter with etch time suggests that the pores formed stabilize at a size of ~ 0.4 nm upon reaction with the potassium permanganate. **d.** Example of pores found in graphene, monovacancy, 0.5 nm diameter pore, and 1 nm diameter pore. Scale bars are 0.5 nm. X-ray photoelectron spectroscopy of pristine graphene and graphene bombarded and etched for 120 min shows formation of C=O and C-O bonds during etching.

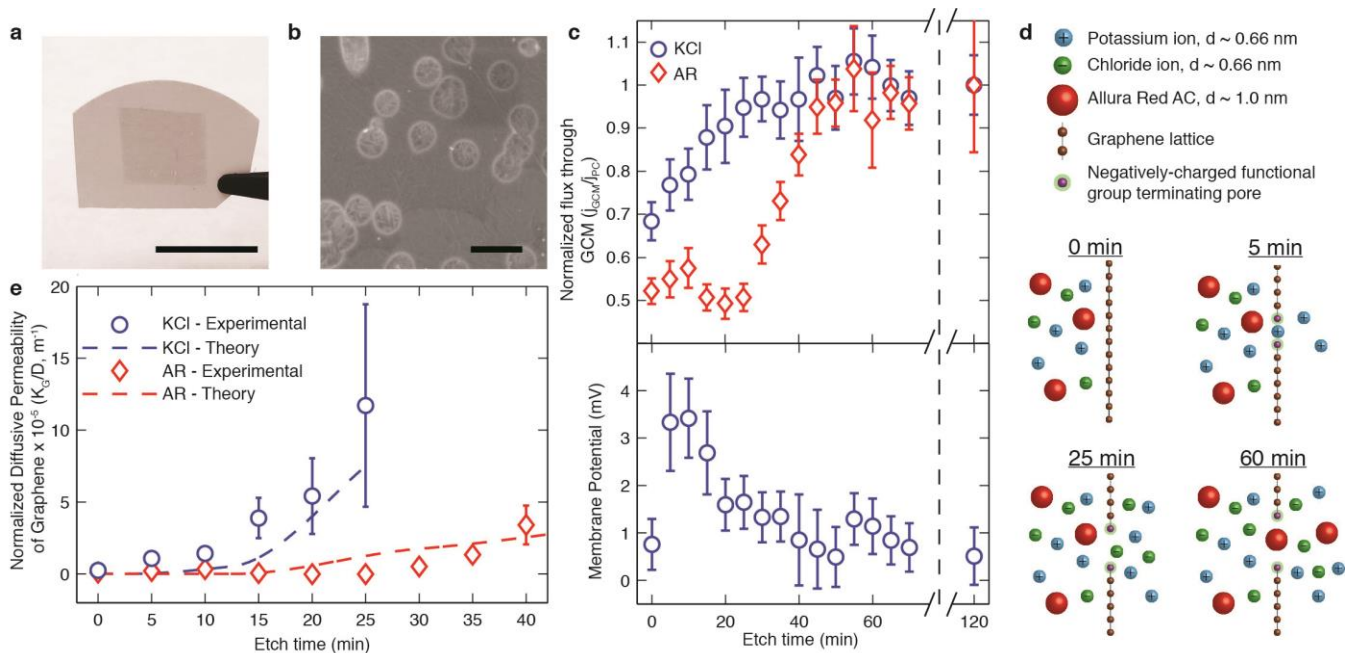


Figure 5. Experimental transport measurements through graphene membranes. **a**, Graphene composite membrane consisting of graphene ($\sim 1 \text{ cm}^2$) fixed to a polycarbonate track etch membrane with 200 nm pores fabricated using direct transfer process described in ref.²⁴. Photograph and **b**, SEM image are shown. Scale bars are 1 cm and 500 nm, respectively. **c**. Diffusive flux through the graphene membranes normalized by flux at 120 min etch time and membrane potential measurements (0.5 M KCl/0.1667 M KCl) demonstrate selective nature of created pores. Error bars represent 95% CI on three measurements from Student's t-Distribution. **d**. Schematic of different regimes of selective transport. At 0 min, transport of both KCl and Allura Red AC occurs only through intrinsic defects and cracks in the graphene. At 5 min, the increase in membrane potential suggests the emergence of modest selectivity in the transport of the positively-charged potassium ion over the negatively-charge chloride ion. At 25 min, the electrostatic effects have diminished and the created pores are larger than KCl yet smaller than Allura Red AC molecules, permitting the transport of KCl yet blocking the transport

of Allura Red AC. After 60 min of etching, the pores are now large enough to permit transport of Allura Red AC across the membrane. **e.** Comparison of the normalized diffusive permeability calculated from experimentally measured diffusive transport and the theoretical permeability based on the pore size distribution from STEM imaging suggests that the created holes are responsible for the selective nature of the membrane. KCl diameter ~ 0.66 nm, Allura Red diameter ~ 1.0 nm. Error bars represent uncertainty derived from standard deviation of three transport measurements.

Supporting Information

Extended methods, additional analysis of graphene on TEM grid, transport measurements on non-bombarded graphene and bare PCTE membranes, and calculation of graphene permeability. This material is available free of charge via the Internet at <http://pubs.acs.org>.

Corresponding Author

*Corresponding Author. Email: karnik@mit.edu

Author Contributions

S.C.O. and R.K. designed the experiments. S.C.O. performed the experiments. S.C.O. and J.C.I. performed STEM imaging. S.C.O., M.S.H.B. and R.K. developed the models. Y.S. and J.K. synthesized the graphene. All authors contributed to data analysis. R.K. supervised the project. S.C.O. and R.K. wrote the paper.

Acknowledgements

The authors would like to thank N. Hadjiconstantinou, T. Jain, and J. Lee for helpful discussions. Graphene composite membrane fabrication and transport measurement

studies were funded by King Fahd University of Petroleum and Minerals in Dhahran, Saudi Arabia through the Center for Clean Water and Clean Energy at MIT and KFUPM under project number R10-CW-09. Ion bombardment, etching, and characterization of porous graphene were supported by the US Department of Energy, Basic Energy Sciences, under award number DE-SC0008059. STEM imaging was supported by ORNL's Shared Research Equipment (ShaRE) User Facility Program (JCI), which is sponsored by the Office of Basic Energy Sciences, the U.S. Department of Energy. Raman spectroscopy and XPS measurements were performed at the Center for Nanoscale Systems (CNS), a member of the National Nanotechnology Infrastructure Network (NNIN), which is supported by the National Science Foundation under NSF award no. ECS-0335765. CNS is part of Harvard University. Ion bombardment and SEM imaging was performed at the MRSEC Shared Experimental Facilities supported by the National Science Foundation under award number DMR-0819762 at MIT.

Notes

The authors declare no competing financial interests.

References

1. Cohen-Tanugi, D.; Grossman, J. *Nano Lett.* **2012**, *12*, (7), 3602-3608.
2. Konatham, D.; Yu, J.; Ho, T. A.; Striolo, A. *Langmuir* **2013**, *29*, 11884–11897.
3. Zhao, S.; Xue, J.; Kang, W. *J. Chem. Phys.* **2013**, **139**, 114702.
4. Jiang, D.; Cooper, V.; Dai, S. *Nano Lett.* **2009**, *9*, (12), 4019-4024.
5. Du, H.; Li, J.; Zhang, J.; Su, G.; Li, X.; Zhao, Y. *J. Phys. Chem. C* **2011**, *115*, (47), 23261-23266.

6. Bunch, J.; Verbridge, S.; Alden, J.; van der Zande, A.; Parpia, J.; Craighead, H.; McEuen, P. *Nano Lett.* **2008**, *8*, (8), 2458-2462.
7. Suk, M.; Aluru, N. *J. Phys. Chem. Lett.* **2010**, *1*, (10), 1590-1594.
8. Sint, K.; Wang, B.; Kral, P. *J. Am. Chem. Soc.* **2009**, *131*, (27), 9600-9600.
9. Koenig, S.; Wang, L.; Pellegrino, J.; Bunch, J. *Nat. Nanotech.* **2012**, *7*, (11), 728-732.
10. Garaj, S.; Hubbard, W.; Reina, A.; Kong, J.; Branton, D.; Golovchenko, J. *Nature* **2010**, *467*, (7312), 190-193.
11. Garaj, S.; Liu, S.; Golovchenko, J.; Branton, D. *Proceedings of the National Academy of Sciences of the United States of America* **2013**, *110*, (30), 12192-12196.
12. Merchant, C.; Healy, K.; Wanunu, M.; Ray, V.; Peterman, N.; Bartel, J.; Fischbein, M.; Venta, K.; Luo, Z.; Johnson, A.; Drndic, M. *Nano Lett.* **2010**, *10*, (8), 2915-2921.
13. Nair, R.; Wu, H.; Jayaram, P.; Grigorieva, I.; Geim, A. *Science* **2012**, *335*, (6067), 442-444.
14. Kim, H. W.; Yoon, H. W.; Yoon, S.-M.; Yoo, B. M.; Ahn, B. K.; Cho, Y. H.; Shin, H. J.; Yang, H.; Paik, U.; Kwon, S.; Choi, J.-Y.; Park, H. B. *Science* **2013**, *342*, (6154), 91-95.
15. Li, H.; Song, Z.; Zhang, X.; Huang, Y.; Li, S.; Mao, Y.; Ploehn, H. J.; Bao, Y.; Yu, M. *Science* **2013**, *342*, (6154), 95-98.
16. Han, Y.; Xu, Z.; Gao, C. *Advanced Functional Materials* **2013**, *23*, (29), 3693-3700.

17. Schneider, G.; Kowalczyk, S.; Calado, V.; Pandraud, G.; Zandbergen, H.; Vandersypen, L.; Dekker, C. *Nano Lett.* **2010**, *10*, (8), 3163-3167.
18. Liu, H.; He, J.; Tang, J.; Liu, H.; Pang, P.; Cao, D.; Krstic, P.; Joseph, S.; Lindsay, S.; Nuckolls, C. *Science* **2010**, *327*, (5961), 64-67.
19. Cheng, Y.; Kaloni, T.; Zhu, Z.; Schwingenschlogl, U. *Appl. Phys. Lett.* **2012**, *101*, (7).
20. Wu, S.; Yang, R.; Shi, D.; Zhang, G. *Nanoscale* **2012**, *4*, (6), 2005-2009.
21. Liu, L.; Ryu, S.; Tomasik, M.; Stolyarova, E.; Jung, N.; Hybertsen, M.; Steigerwald, M.; Brus, L.; Flynn, G. *Nano Lett.* **2008**, *8*, (7), 1965-1970.
22. Bai, J.; Zhong, X.; Jiang, S.; Huang, Y.; Duan, X. *Nat. Nanotechnol.* **2010**, *5*, (3), 190-194.
23. Russo, C. J.; Golovchenko, J. A. *P. Nat. Acad. Sci. USA* **2012**, *109*, (16), 5953-5957.
24. O'Hern, S.; Stewart, C.; Boutilier, M.; Idrobo, J.; Bhaviripudi, S.; Das, S.; Kong, J.; Laoui, T.; Atieh, M.; Karnik, R. *Acs Nano* **2012**, *6*, (11), 10130-10138.
25. Compagnini, G.; Giannazzo, F.; Sonde, S.; Raineri, V.; Rimini, E. *Carbon* **2009**, *47*, (14), 3201-3207.
26. Lehtinen, O.; Kotakoski, J.; Krasheninnikov, A.; Keinonen, J. *Nanotechnology* **2011**, *22*, (17).
27. Schlogl, R., Carbons. In *Handbook of Heterogeneous Catalysis*, Ertl, G.; Knozinger, H.; Weitkamp, J., Eds. Wiley VHC: Weinheim, Germany, 1997; Vol. 1, pp 138-191.
28. Dash, S.; Patel, S.; Mishra, B. *Tetrahedron* **2009**, *65*, (4), 707-739.

29. Kosynkin, D.; Higginbotham, A.; Sinitiskii, A.; Lomeda, J.; Dimiev, A.; Price, B.; Tour, J. *Nature* **2009**, *458*, (7240), 872-U5.
30. Malard, L.; Pimenta, M.; Dresselhaus, G.; Dresselhaus, M. *Phys. Rep.* **2009**, *473*, (5-6), 51-87.
31. Banhart, F.; Kotakoski, J.; Krasheninnikov, A. *Acs Nano* **2011**, *5*, (1), 26-41.
32. Mehmood, F.; Pachter, R.; Lu, W.; Boeckl, J. *Journal of Physical Chemistry C* **2013**, *117*, (20), 10366-10374.
33. Rangel, N.; Sotelo, J.; Seminario, J. *J. Chem. Phys.* **2009**, *131*, (3).
34. Wang, S.; Wang, R.; Liu, X.; Wang, X.; Zhang, D.; Guo, Y.; Qiu, X. *Journal of Physical Chemistry C* **2012**, *116*, (19), 10702-10707.
35. Wang, S.; Wang, R.; Liu, X.; Wang, X.; Zhang, D.; Guo, Y.; Qiu, X. *J. Phys. Chem. C* **2012**, *116*, (19), 10702-10707.
36. Li, X. S.; Cai, W. W.; An, J. H.; Kim, S.; Nah, J.; Yang, D. X.; Piner, R.; Velamakanni, A.; Jung, I.; Tutuc, E.; Banerjee, S. K.; Colombo, L.; Ruoff, R. S. *Science* **2009**, *324*, (5932), 1312-1314.
37. Xuan, Y.; Wu, Y.; Shen, T.; Qi, M.; Capano, M.; Cooper, J.; Ye, P. *Applied Physics Letters* **2008**, *92*, (1).
38. Hilal, N.; Al-Zoubi, H.; Darwish, N.; Mohammad, A.; Abu Arabi, M. *Desalination* **2004**, *170*, (3), 281-308.
39. Mao, H.; Lu, Y.; Lin, J.; Zhong, S.; Wee, A.; Chen, W. *Progress in Surface Science* **2013**, *88*, (2), 132-159.
40. Chua, C.; Pumera, M. *Chemical Society Reviews* **2013**, *42*, (8), 3222-3233.

41. Lehtinen, O.; Kotakoski, J.; Krasheninnikov, A.; Tolvanen, A.; Nordlund, K.; Keinonen, J. *Physical Review B* **2010**, 81, (15).
42. Guo, B.; Liu, Q.; Chen, E.; Zhu, H.; Fang, L.; Gong, J. *Nano Letters* **2010**, 10, (12), 4975-4980.
43. Lin, Y.; Jin, C.; Lee, J.; Jen, S.; Suenaga, K.; Chiu, P. *ACS Nano* **2011**, 5, (3), 2362-2368.
44. Krivanek, O.; Corbin, G.; Dellby, N.; Elston, B.; Keyse, R.; Murfitt, M.; Own, C.; Szilagy, Z.; Woodruff, J. *Ultramicroscopy* **2008**, 108, (3), 179-195.